THE JOURNAL OF PHYSICAL CHEMISTRY C

Article

Cite This: J. Phys. Chem. C 2019, 123, 24963−24972

pubs.acs.org/JPCC

Spin−Orbit Torque and Spin Hall Effect-Based Cellular Level Therapeutic Spintronic Neuromodulator: A Simulation Study

Kai Wu,*[,†] Diqing Su,[‡] Renata Saha,[†] and Jian-Ping Wang*[,†]

[†]Department of Electrical and Computer Engineering, and [‡]Department of Chemical Engineering and Material Science, University of Minnesota, Minneapolis, Minnesota 55455, United States

Supporting Information

ABSTRACT: Artificial modulation of a neuronal subset through ion channels activation can initiate firing patterns of an entire neural circuit *in vivo*. As nanovalves in the cell membrane, voltage-gated ion channels can be artificially controlled by the electric field gradient that is caused by externally applied time varying magnetic fields. Herein, we theoretically investigate the feasibility of modulating neural activities by using magnetic spintronic nanostructures. An antiferromagnet/ferromagnet (AFM/FM) structure is explored as neuromodulator. For the FM layer with perpendicular magnetization, stable bidirectional magnetization switching can be achieved by applying in-plane currents through the AFM layer to induce the spin-orbit torque (SOT) due to the spin Hall effect (SHE). This spin-orbit torque neurostimulator (SOTNS) utilizes in-plane charge current pulses to switch the magnetization in the FM layer. The time changing magnetic stray field induces an electric field that modulates the surrounding neurons. The object oriented micromagnetic framework (OOMMF) is used to calculate space- and time-dependent magnetic dynamics of the SOTNS structure. The current-driven magnetization dynamics in the SOTNS has no mechanically moving parts. Furthermore, the size of the SOTNS can be down to tens of nanometers. Thus, arrays of SOTNSs could be fabricated, integrated together, and patterned on a flexible substrate, which gives us much more flexible control of the neuromodulation with cellular resolution.

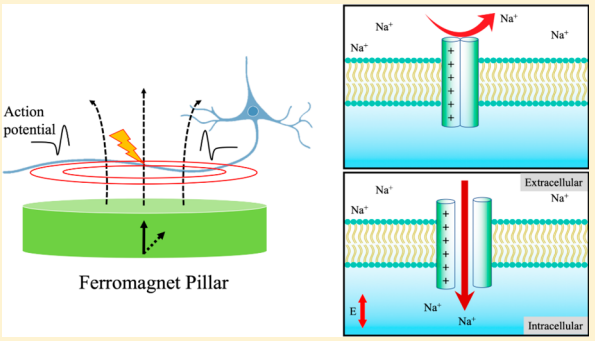

1. INTRODUCTION

Nowadays, technologies for controlled artificial modulation of neuronal activities are recognized as important tools for neural science and engineering. The past three decades have seen a tremendous advance in neuromodulation technologies, including noninvasive approaches such as transcranial magnetic stimulation (TMS) and invasive strategies such as deep brain stimulation (DBS). Each of these emerging approaches has its unique strengths and applications, but also drawbacks and limitations. DBS is an invasive technique in which electrodes are implanted inside the brain permanently to activate deeply located neurons.[1,2] However, glial cell scarring and migration of neighboring astrocytes near the point of stimulating electrodes often lead to increased impedance thereby affecting the effectiveness of this technique.[3−5] Furthermore, DBS electrodes have been observed to be highly MRI incompatible because radio frequencies lead to electrode tip heating causing local apoptosis of neuronal cells; this condition has been extensively reviewed in literature as the "antenna effect".[6,7] On the other hand, TMS is a noninvasive technique in which the brain's electrical environment is modulated by passing strong nonstatic magnetic fields (1.5−3 T) through scalp and skull. These magnetic fields are generated by passing alternating current (AC) through a coil with a ferromagnetic core.[8−10] Following the principles of Faraday's Laws, this magnetic field generates a spatially asymmetric electric field gradient that stimulates the neurons in that vicinity. However, TMS cannot stimulate neurons selectively because it is unable to generate a focused magnetic field which is where DBS electrodes have an advantage. In addition to being bulky in size, TMS cannot activate deeply located neurons since the magnetic field decays exponentially through the skull.

In the quest to exploit the efficiency of both focally stimulating DBS electrodes and magnetic neurostimulators, Bonmassar et al. pioneered neuron stimulations with commercially available submillimeter coils.[11−13] They simulated as well as prototyped microcoils and performed experiments on several animal-models, validating microcoils to be a promising alternative for the existing implantable neurostimulators. However, these micromagnetic stimulating (μMS) coils are capable of effectively stimulating neurons only when the axis of the coils is in parallel to the axis of the axons. This makes μMS coils quite inefficient in terms of directionality as in reality neurons are randomly oriented. Even more, these microcoils have been reported to operate at high power[13] and thereby pose yet another challenge of having

Received: August 7, 2019
Revised: September 2, 2019
Published: September 16, 2019

DOI: 10.1021/acs.jpcc.9b07542
J. Phys. Chem. C 2019, 123, 24963−24972

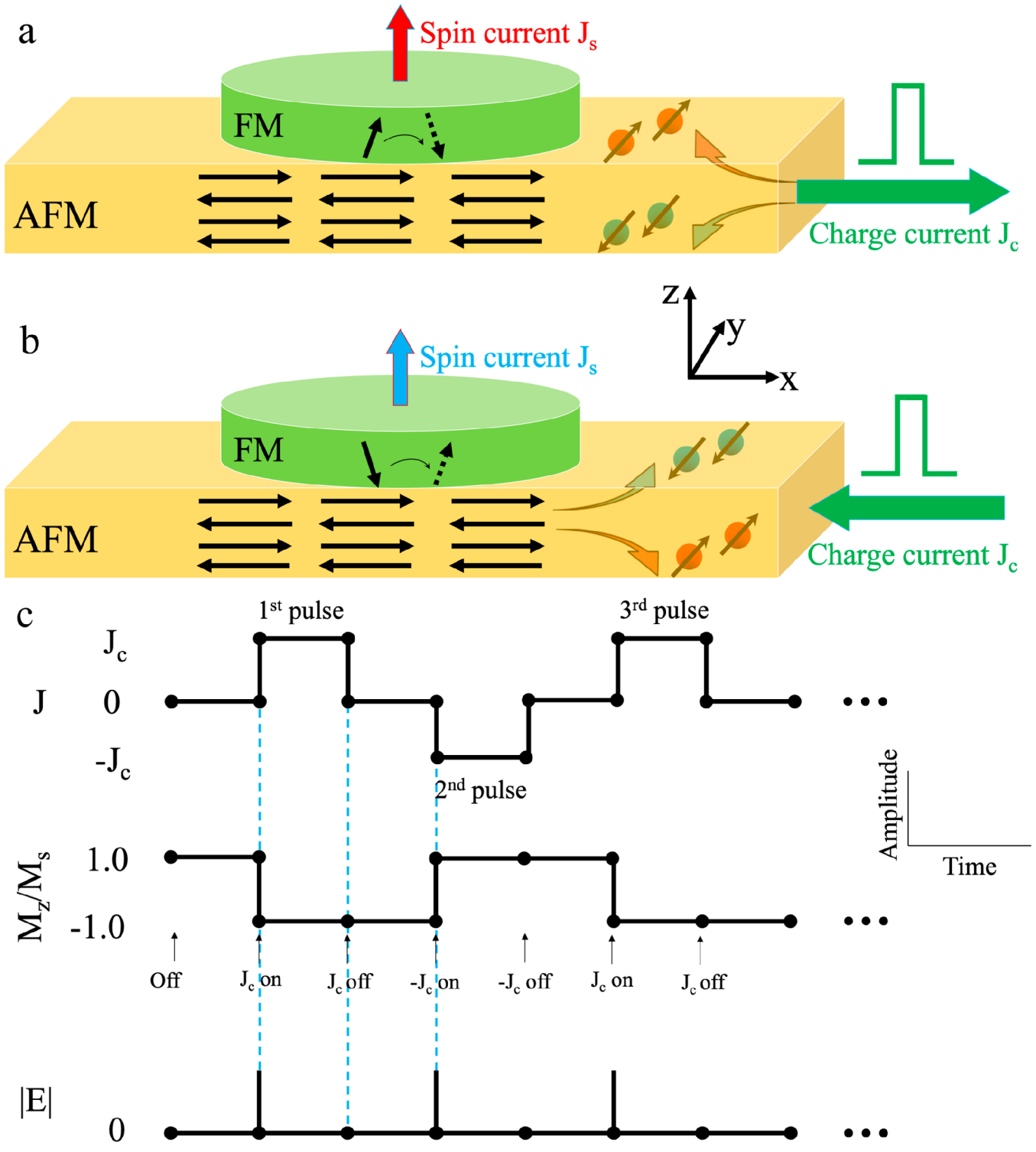

Figure 1. (a and b) Schematics of the antiferromagnet/ferromagnet (AFM/FM) bilayer structure. J_C is the in-plane charge current along the *X*-direction. Exchange bias supplied by AFM allows field-free switching in laterally homogeneous structures. In-plane charge current running in the *X*-direction yields a spin current in the *Z*-direction due to the spin Hall effect, this spin current exerts torques to switch the magnetization of the FM layer. (c) Theoretical switching behavior of the SOTNS model.

detrimental thermal effects on the brain tissues.[14] In this work, we are exploring the feasibility of modulating neural activities by using magnetic spintronic nanostructures. In 2016, Wang et al. filed a patent on a current-driven domain-wall motion along a magnetic nanowire as a possible spintronic neurostimulator.[15] Very recently Saha et al.[16] reported the first proof-of-concept for a magnetic skyrmion-based neurostimulator (SkyNS) where the displacement of skyrmions on a ferromagnet/heavy metal bilayer generates a time-varying magnetic field thereby causing an electric field gradient large enough to trigger neurostimulation. This spin-orbit torque neurostimulator (SOTNS) utilizes in-plane charge current pulses to flip back and forth the magnetization in a ferromagnet nanopillar. As a result, the time varying magnetic

DOI: 10.1021/acs.jpcc.9b07542
J. Phys. Chem. C 2019, 123, 24963−24972

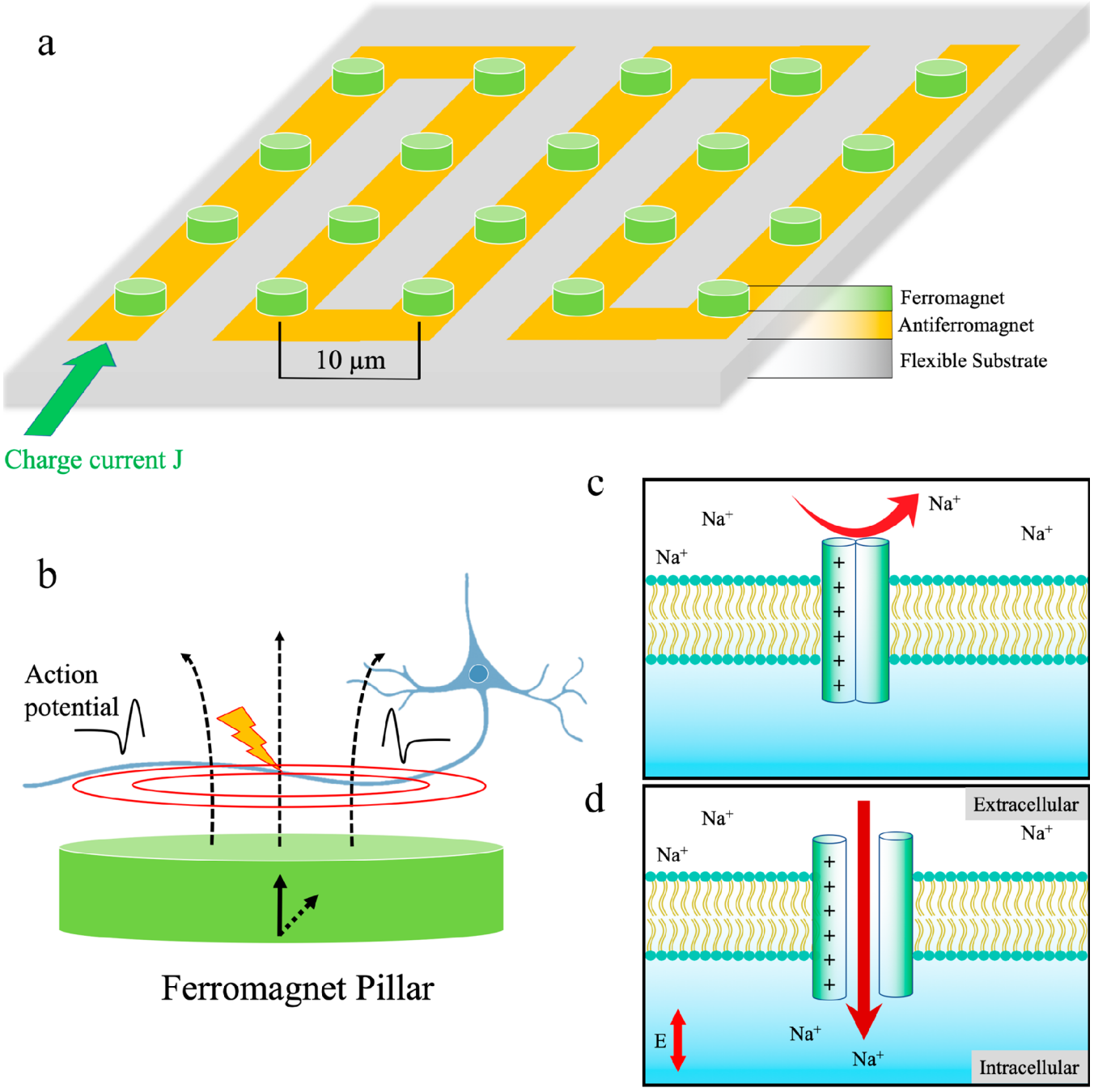

Figure 2. (a) SOTNS arrays integrated on a flexible substrate give us much more flexible control of the neuromodulation. (b) Flipping the magnetization of the FM layer induces an electric field that can modulate the neural activities of nearby neurons, initiating two action potentials on the axon going to opposite ways: the orthodromic and antidromic. (c) Schematic view of voltage-gated sodium channel (VGSC) before a stimulation. The Na^+ channels are in the deactivated state. (d) The VGSC opens upon the onset of an electric field **E**, allowing Na^+ ions to flow into the neuron through the channel. An action potential is initiated.

stray field induces an electric field that modulates the surrounding neurons. Although the magnetic field does not specifically stimulate the neurons, it is highly permeable through biological tissues.[17] Therefore, the indirect electric field generated from it will be free from encapsulation of astrocytes or any other cells. SOTNS is a nanoscale device, operating on a current of 0.367−2.581 mA and a power of 6.34−313.5 μW capable of stimulating neurons in any orientations as opposed to μMS coils. In addition, the current driven magnetization dynamics in SOTNS has no mechanically moving parts. Furthermore, the ability to fabricate magnetic nanostructures allows neurostimulation at the level of single cells and potentially at the synapse level.

2. THEORY

2.1. Physical Model of the SOTNS. Recent studies have shown that by applying an in-plane charge current J_c to a heterostructure with large spin−orbit interaction and structural inversion asymmetry results in a spin−orbit torque (SOT), which in turn induces the magnetization switching in the adjacent perpendicular ferromagnetic layer.[18] A typical

DOI: 10.1021/acs.jpcc.9b07542
J. Phys. Chem. C 2019, 123, 24963−24972

structure consists of a nonmagnet/ferromagnet (NM/FM) bilayer, in which the NM layer is a spin Hall channel, and it generates the transverse spin current J_s. This spin current is polarized along the in-plane direction and it accumulates at the interface between NM and FM layers exerting a Slonczewski-like torque (SLT) to switch the magnetization of the FM layer. The ratio of spin current to the charge current is represented by the spin Hall angle (SHA). Usually a small symmetry-breaking bias field along the charge current direction is needed for deterministic SOT switching.[19] However, it is impractical to apply an external magnetic field in the neuromodulation applications. Recently, field-free SOT switching methods have been reported by introducing interlayer exchange coupling,[20−22] tilted magnetic anisotropy,[23] interplay of spin-orbit and spin-transfer torques,[24] etc.

Herein, we are exploring the antiferromagnet/ferromagnet (AFM/FM) structure as neuromodulator (see Figure 1a,b), where the AFM layer supplies an in-plane exchange bias field on the adjacent FM layer and meanwhile generates SOT that enables the purely electrical deterministic switching of perpendicular magnetization without any external bias field. For a system with single-domain state and perpendicular magnetic anisotropy (PMA) on top of an AFM layer with a current-in-plane (CIP) geometry, the critical current density J_C for a deterministic magnetization switching is written as[25]

$$J_C = \frac{2e\mu_0}{\hbar}\frac{M_S t_F}{\theta_{SH}^{\text{eff}}}\left(\frac{H_K^{\text{eff}}}{2} - \frac{H_X}{\sqrt{2}}\right) \tag{1}$$

$$H_K^{\text{eff}} = H_K - N_d M_s \tag{2}$$

where θ_{SH}^{eff} is the effective spin Hall angle, M_S, t_F, H_K^{eff}, and H_K are the saturation magnetization, thickness, effective anisotropy field, and perpendicular anisotropy field of the FM layer, respectively, and H_X is the exchange bias field.

One advantage of this SOTNS is that there are no mechanical moving parts in this system, the magnetization (as well as the direction of magnetic field) of the FM layer can flip back and forth by changing the charge current directions as shown in Figure 1a,b, where an in-plane charge current J_c passing through the AFM layer is converted into a perpendicular spin current J_s due to the spin Hall effect (SHE).

Another advantage of SOTNS is that since the magnetic field is highly permeable through biological tissues due to their similar permeability to that of the free space,[26] it would spare the device from being encapsulated by astrocytes or glial cells as is often the case for electrical implants.[4,5] On the basis of the Maxwell-Faraday law, a rapidly fluxing magnetic field induces an electromotive force (emf):

$$\oint \mathbf{E}\cdot d\mathbf{l} = -\iint \frac{\partial \mathbf{B}}{\partial t}\cdot d\mathbf{S} \tag{3}$$

where $\mathbf{B}$ is the magnetic field, $\mathbf{E}$ is the electric field, $\mathbf{l}$ is the contour, and $\mathbf{S}$ is the surface.

Figure 1c describes the theoretical switching of the magnetization M_Z (the Z-component of magnetization M) from $+Z$ to $-Z$ directions and vice versa depending on the charge current direction applied during the time window. Upon the onsets of magnetization M_Z flipping from $+Z$ to $-Z$ directions (or $-Z$ to $+Z$ directions, see the black arrows in Figure 2b), the time-varying magnetic flux induces local electric field $\mathbf{E}$ (see the red circles in Figure 2b).

The size of SOTNS can be down to tens of nanometers, thus, arrays of SOTNSs could be fabricated and integrated together as shown in Figure 2a. The SOTNSs patterned on a flexible substrate will give us much more flexible control of the neuromodulation. While this proof-of-concept device includes a single chip, dozens of chips could be run by the same electronics. These devices can then be assembled to make a full 3-D array. This is similar in concept to the work by Wise et al.,[27,28] but with spintronic nanodevices and nanofabrication technology, the size of each neuromodulator could shrink from micrometers to nanometers.

2.2. Biological Model. Neurons encode information with electrical signals and transmit the information to other neurons by synapses. When an external oscillating electric field is applied,[26] the charged ions are triggered into a coherently forced vibration of a specific amplitude which is in phase with the applied electric field. The coherently forced vibration of these ions generates an electrostatic interaction which causes the voltage-gated ion channels to open and close thereby allowing ions to move in and out of the ion channels. This activity disrupts the electrochemical balance between the intracellular and extracellular matrix of the neuron cells. This phenomenon is better termed as action potential. Therefore, the external electric field being the cause, action potential is the effect. The action potential is a very important electrical signal that occurs when the membrane potential of a specific axon location rapidly rises and falls. Action potentials are generated mainly by specific types of ion channels embedded in a cell's membrane. The principle ions involved in an action potential are Na^+ and K^+ ions where Na^+ ions enter the cell and K^+ ions move out of the cell.

These ion channels are pore-forming membrane proteins that allow ions to pass through the channel pore. They underlie the resting membrane potential, action potentials, and other electrical signals by gating the flow of ions across the cell membrane. There are three main groups of ion channels, they can be classified by the nature of their gating: voltage-gated, ligand-gated, and mechanically gated. To understand the neural circuits and behaviors, many external means have been used to activate ion channels, such as the ultrasonic control of neural activities through the mechanically gated ion channels,[29,30] the chemical neuromodulation exerting on the ligand-gated ion channels that delivers drug invasively (e.g., memantine and agomelatine) for brain disorder treatments,[31,32] and the TMS and DBS techniques which artificially control the voltage-gated ion channels. As the ion channels open by different means, specific types of ions pass through the channels down their electrochemical gradient, initiating an action potential. If the stimulation is exerting on the ion channels at the axon hillock region, then one action potential will be initiated and travel down the axon (orthodromic). If the stimulation is exerted in the middle of an axon, two action potentials will be initiated and propagate along opposite directions (antidromic and orthodromic). Figure 2b shows the latter case in which the electric field generated by the SOTNS is exerting in the middle of an axon.

Take the voltage-gated sodium channel (VGSC) as an example. As shown in Figure 2c, before a stimulation, the axonal membrane is at its resting potential and the Na^+ channels are in the deactivated state, blocking the Na^+ ions in the extracellular side. During one cycle of neuromodulation process, an electric field $\mathbf{E}$ is generated by SOTNS locally. In response to the electric field, the VGSCs open (see Figure 2d),

DOI: 10.1021/acs.jpcc.9b07542
J. Phys. Chem. C 2019, 123, 24963−24972

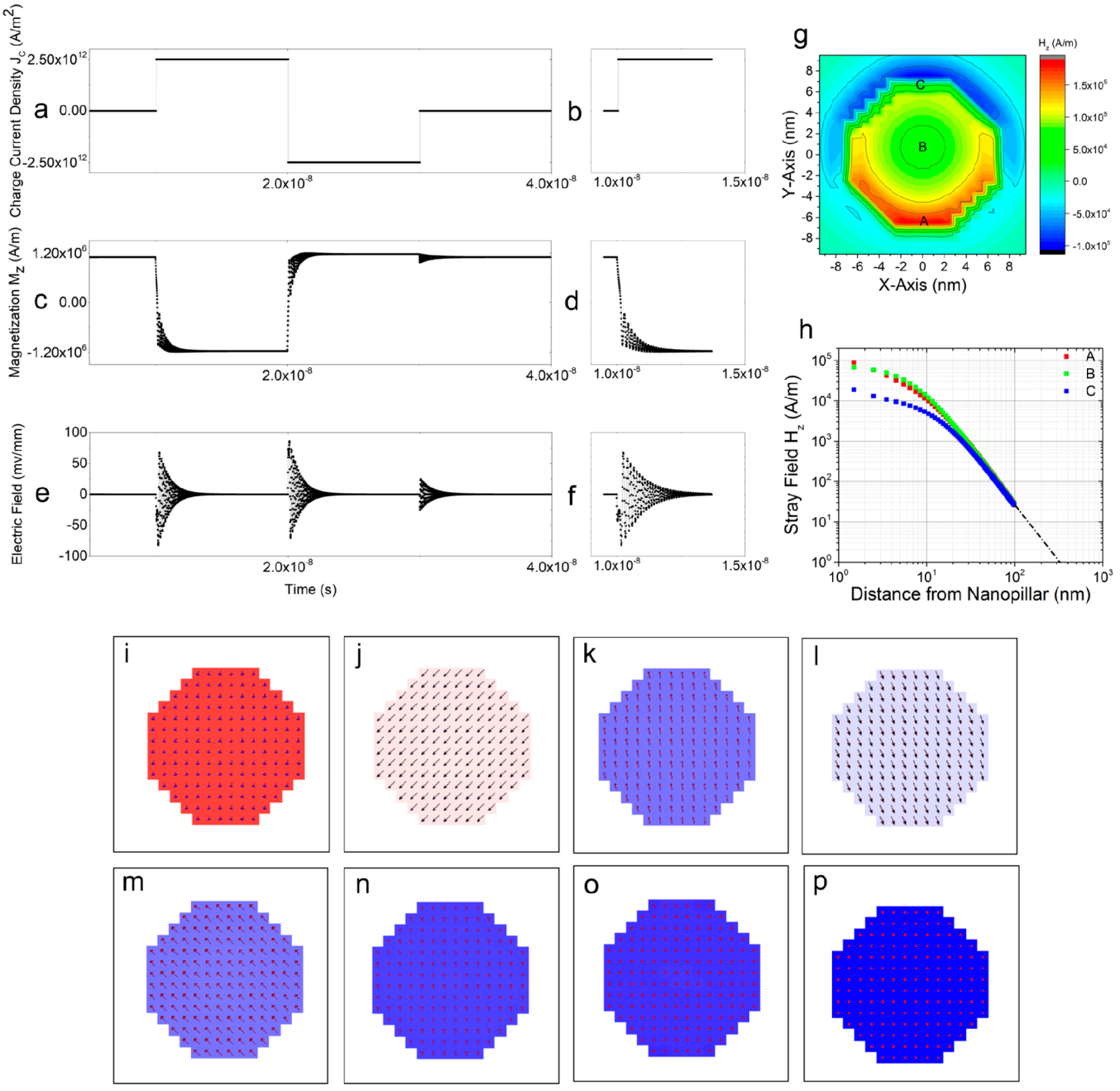

Figure 3. (a) Applied charge current pulses. $|J_C| = 2.5 \times 10^{12}\ A/m^2$, ± signs indicate J_C flows along $\pm X$ axis. (b) Charge current + J_C is on at 10 ns. (c) Magnetization component $|M_z| \sim 1.2 \times 10^6$ A/m, ± signs indicate M_z points to $\pm Z$ direction. (d) Flipping M_z from $+Z$ direction to $-Z$ direction by a charge current pulse + J_C within 3 ns. (e) Calculated real-time electric field based on Maxwell−Faraday law. (f) Real-time electric field within 3 ns of charge current pulse + J_C. (g) Magnetic stray field component H_z on the top surface of 14 nm FM nanopillar when the magnetization is fully switched ($M_z/M_s = 1$). Points A and C are at the edge of nanopillar, and point B is in the center of nanopillar. (h) Magnetic stray field component H_z attenuates from top surface of nanopillar to a distance of 100 nm from surface along Z-axis. (i−p) simulated magnetization evolution in a 14 nm diameter FM nanopillar at $\triangle t$ = 0, 0.05 ns, 0.13 ns, 0.20 ns, 0.28 ns, 0.90 ns, 1.21 ns, and 2.06 ns after applying the charge current pulse.

allowing Na^+ ions to flow into the neuron through the channels, causing the voltage across the neuronal membrane to increase. The increase in membrane potential constitutes the rising phase of an action potential.

2.3. Micromagnetic Simulations on SOTNS. In this work, the object oriented micromagnetic framework (OOMMF)[33] is used to calculate space- and time-dependent magnetic dynamics of the SOTNS structure. For the FM layer with perpendicular magnetization, stable bidirectional magnetization switching can be achieved by applying in-plane currents through the AFM layer to induce the SOT under an exchange bias field. Many experimental works have revealed that the SLT (τ_{SLT}) is considered to be responsible for the SOT switching.[19,34−37] The Landau−Lifshitz−Gilbert (LLG) equation including the SOT term is expressed as

$$\frac{\partial \mathbf{m}}{\partial t} = -\gamma_0 \mu_0 \mathbf{m} \times \mathbf{H}_{eff} + \alpha \mathbf{m} \times \frac{\partial \mathbf{m}}{\partial t} + \tau_{SLT} \quad (4)$$

DOI: 10.1021/acs.jpcc.9b07542
J. Phys. Chem. C 2019, 123, 24963−24972

$$\tau_{SLT} = \gamma_0 \mu_0 \tau_d \mathbf{m} \times (\mathbf{m} \times \boldsymbol{\sigma}) \quad (5)$$

where $\mathbf{m} = \frac{\mathbf{M}}{M_s}$ is the unit magnetization vector with M_s being the saturation magnetization, $\mathbf{H}_{eff}$ is an effective magnetic field including an effective perpendicular anisotropy field $\mathbf{H}_{K,eff}$ (= $H_K - N_d M_s$) is an external exchange bias field H_X, and the interfacial anisotropic exchange field due to the Dzyaloshinskii–Moriya interaction (DMI), γ_0 is the gyromagnetic ratio, α is the Gilbert damping parameter, τ_{SLT} is the SLT term, $\tau_d = \frac{\hbar \theta_{SH}^{eff} J_c}{2 e \mu_0 M_s t_F}$ is the magnitude of SLT, and $\boldsymbol{\sigma}$ is the direction of spin polarization. The polarity of the SOT torque is determined by the direction of the in-plane current J_c.

PtMn is chosen as the AFM layer due to its higher spin Hall angle compared to other CuAu-I-type AFM[38−40] such as IrMn, PdMn, and FeMn. The spin Hall angle θ_{SH}^{eff} of PtMn varies from 0.06 up to 0.24 in different studies.[38,39,41] Herein, we assume θ_{SH}^{eff} = 0.12. The PMA is achieved only in a limited range of CoFeB layer thickness; therefore, we fix the thickness at 1 nm which is within the range. The structure of a Hall bar stack is assumed, from the substrate side, Ta(5 nm)/PtMn(9 nm)/CoFeB(1 nm)/MgO(1.6 nm)/Ta(2 nm).[22,39,41,42] The saturation magnetization of the CoFeB layer is $M_S = 1.2 \times 10^6$ A/m.[18] For this sufficiently thin CoFeB layer, the PtMn (AFM)/CoFeB (FM)/MgO structure induces a strong perpendicular easy axis with an effective anisotropy field H_K^{eff} between 120 mT and 500 mT along the Z-axis,[21,22,43−45] and the anisotropy field H_K is between 1.5 and 2 T. The exchange bias field H_X is assumed to be 15 mT along X-axis, which can be achieved by annealing at 300 °C under an in-plane magnetic field of 1.2 T along the Y-axis for 2 h[22] (Lau et al.[20] reached an exchange bias up to 50 mT by replacing MgO with Ru). Besides, to ensure the biocompatibility of this SOTNS implant, we plan on adapting the process as recently proposed by Moretti et al.,[46] where a physical vapor deposited a trilayer of $SiO_2/Si_3N_4/SiO_2$ on a relatively biotoxic environment of magnetic tunnel junction (MTJ) stack ensured complete neurophysiological activity of cultured neuron cells for more than 30 days without even altering the device performance.

3. RESULTS AND DISCUSSION

3.1. SOT Switching of 14 nm FM Nanopillar. Herein, we conducted the OOMMF simulations on the CIP geometry AFM/FM nanostructure mentioned in the foregoing sections. In-plane charge current pulses are applied through the AFM layer. The spin Hall torque is directed along $\boldsymbol{m} \times (\boldsymbol{m} \times \boldsymbol{\sigma})$. The magnetization dynamics of the FM nanopillar with a diameter of 14 nm and thickness t_F = 1 nm (denoted as FM14-SOTNS in this paper) is monitored. Figure 3(a–f) show the time-dependent change of the charge current pulses, the Z-component magnetization of the FM14-SOTNS structure, and the calculated electric field on the surface of FM14-SOTNS. Electric fields are generated during the magnetization switching process. Significant precessional motions are observed when the charge current switches direction or turns on/off, which is because the magnetization direction deviates from its equilibrium direction (i.e., the perpendicular easy axis). The precessional motions induce high-frequency electric field with magnitudes between 0 and 70 mV/mm as shown in Figure 3e. Figure 3f is an enlarged view of one electric field stimulus pulse with a pulse width of ∼2 ns and an intensity of 5–70 mV/mm. The stimulus frequency of electric field pulses can be controlled by setting the charge current switching frequency between 60 and 200 Hz.

The magnitude distribution of the Z-component of a magnetic stray field, H_z, from the surface of FM14-SOTNS is recorded in Figure 3g. Figure 3h shows that the magnetic stray field decays with the distance from the nanopillar surface to a distance of 100 nm along the Z direction. The trend line shows that H_z drops to 1 A/m at a distance of around 300 nm. Figures 3i–p are the magnetization evolutions of FM14-SOTNS after applying the charge current pulse. Each arrow represents an area of 1 nm × 1 nm. Magnetization in the FM14-SOTNS flips from the +Z direction to the −Z direction within 2 ns. Switching is completed by involving the SOT and DMI driven domain wall motion. The parameters used in this OOMMF simulation are listed in Table 1.

Table 1. Simulation Parameters of SOT Switching of CoFeB Nanopillar

parameter	description	values[a]
nanopillar dimensions	diameter × thickness	112 nm × 1 nm (14 nm × 1 nm)
cell size	length × width × thickness	1 nm × 1 nm × 1 nm
γ_0	gyromagnetic ratio	2.211×10^5 m/A·s
α	gilbert damping factor	0.02
A	exchange constant	20×10^{-12} J/m
M_S	saturation magnetization	1.2×10^6 A/m
J_C	charge current density applied in this simulation[b]	2.2×10^{12} A/m^2 (2.5×10^{12} A/m^2)
θ_{SH}^{eff}	spin hall angle	0.12
H_K	perpendicular anisotropy field	1.5 T
H_X	exchange bias field	15 mT
DMI	Dzyaloshinskii–Moriya interaction factor	0.5 mJ/m^2

[a]The parameters used in the simulation on SOT switching of the 14 nm nanopillar are listed in the parentheses. A smaller nanopillar requires larger charge current density J_C to flip its magnetization, and the switching process generates a smaller emf. [b]The critical current density with respect of demagnetization field can be found in the Supporting Information.

3.2. SOT Switching of 112 nm FM Nanopillar. In the foregoing section, we discussed the SOT-based magnetization switching behavior in a FM14-SOTNS structure with a diameter of 14 nm, where it is in the single domain regime. We observed that the switching behavior in the device can be described by one macrospin. In this section, we increased the diameter of FM nanopillar to 112 nm while keeping the thickness 1 nm (denoted as FM112-SOTNS in this paper), entering the nucleation dominated regime. The time evolutions of charge current, Z-component magnetization in the FM nanopillar, and calculated electric field are plotted in Figure 4a–f. During one magnetization switch cycle (from +Z to −Z direction or vice versa), the precessional motions of the magnetization in the FM nanopillar induce a high frequency electric field with magnitudes between 0 and 200 mV/mm as shown in Figure 4e. Figure 4f is an enlarged view of one electric field stimulus pulse with a pulse width of ∼3 ns and an intensity of 5–200 mV/mm.

The Z-component stray field pattern and the stray field decay rate along the Z direction distances are plotted in Figure 4g,h. The trend line shows that H_z drops to 1 A/m at a distance of around 6 μm. In addition, as the FM nanopillar

DOI: 10.1021/acs.jpcc.9b07542
J. Phys. Chem. C 2019, 123, 24963−24972

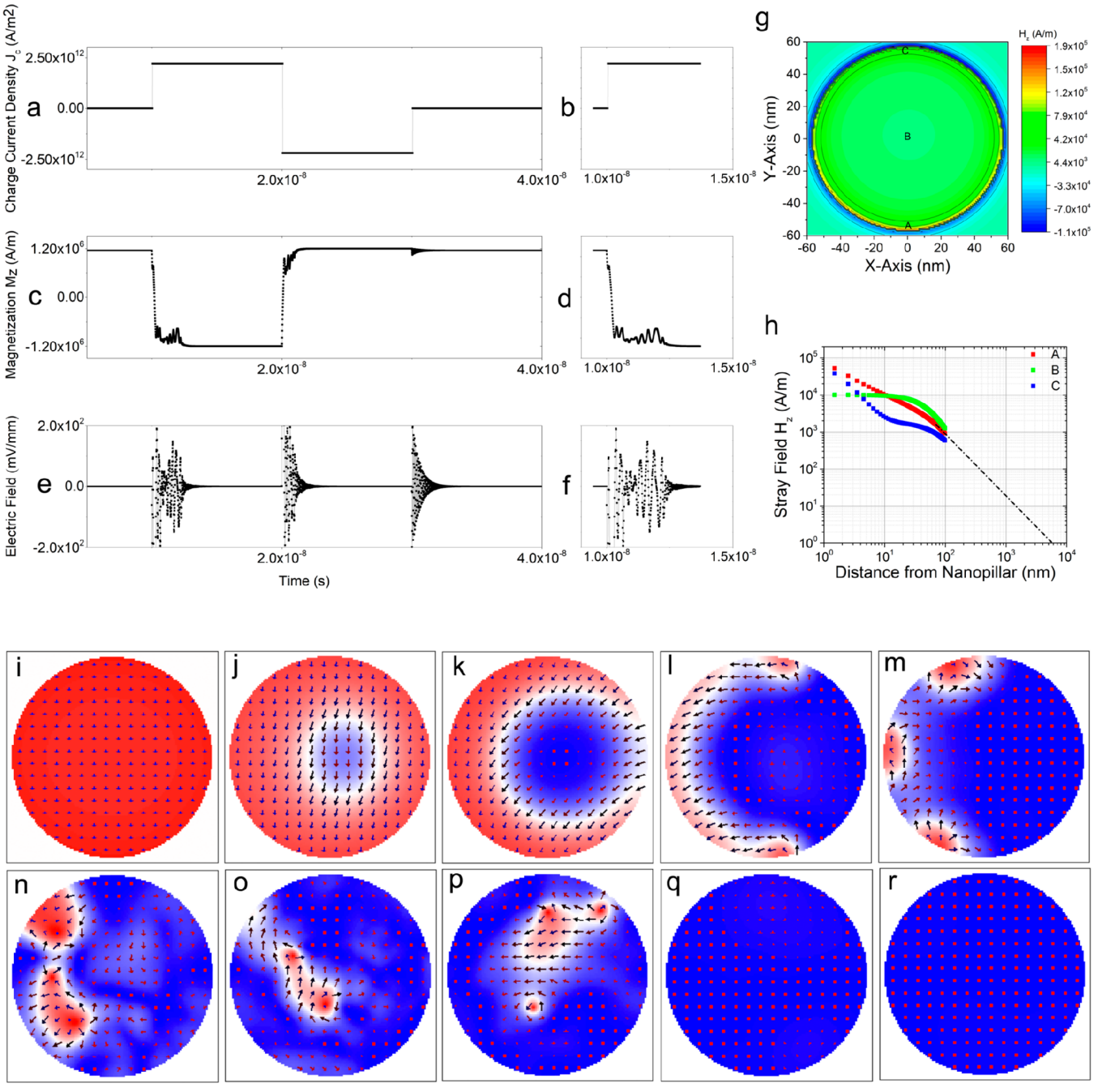

Figure 4. (a) Applied charge current pulses. $|J_C| = 2.2 \times 10^{12}$ A/m^2, ± signs indicate J_C flows along $\pm X$ axis. (b) Charge current + J_C is on at 10 ns. (c) Magnetization component $|M_z| \sim 1.2 \times 10^6$ A/m, ± signs indicate M_z points to $\pm Z$ direction. (d) Flipping M_z from the $+Z$ direction to the $-Z$ direction by a charge current pulse + J_C within 3 ns. (e) Calculated real-time electric field based on Maxwell−Faraday law. (f) Real-time electric field within 3 ns of charge current pulse + J_C. (g) Magnetic stray field component H_z on the top surface of 112 nm FM nanopillar when the magnetization is fully switched ($M_z/M_s = 1$). Points A and C are at the edge of the nanopillar, and point B is in the center of the nanopillar. (h) Magnetic stray field component H_z attenuates from the top surface of nanopillar to a distance of 100 nm from the surface along the Z-axis. The trend line shows that H_z drops to 1 A/m at a distance of around 5 μm. (i−r) simulated magnetization evolution in a 112 nm diameter FM nanopillar at $\triangle t$ = 0, 0.12 ns, 0.20 ns, 0.27 ns, 0.35 ns, 0.42 ns, 0.50 ns, 0.65 ns, 2.79 ns, and 2.94 ns after applying the charge current pulse.

diameter increases from 14 to 112 nm, the overall time for a complete magnetization flip (from + Z to − Z direction or vice versa) increases from 2 to 3 ns. Figure 4 panels i−r show the magnetization evolution of FM112-SOTNS structure vs time. Each arrow represents an area of 7 nm × 7 nm. Magnetization in 112 nm FM nanopillar flips from $+Z$ direction to $-Z$ direction within 3 ns. Switching is completed by involving SOT and DMI driven domain wall motion. Initially, the magnetization of FM is pointing up represented by red pixels in Figure 4i. Upon the application of the charge current, a reverse domain is first nucleated near the center of the pillar (see Figure 4j) followed by the expansion of the domain as shown in Figure 4k−m. The full switching of the magnetization in the FM layer is via the joint action of SOT and DMI. The switching mode of FM112-SOTNS is the nucleation type, which is very different from the FM14-SOTNS from Figure

DOI: 10.1021/acs.jpcc.9b07542
J. Phys. Chem. C 2019, 123, 24963−24972

3i−p where the magnetization switching mode is a single domain type. The local magnetization at the edges tilts because the interfacial DMI imposes boundary conditions at the edge of the FM layer.[47,48]

The parameters used in this simulation are listed in Table 1.

The induced electric field is biphasic in nature and persists for several nanoseconds which is 2 ns for the 14 nm nanopillar and 3 ns for the 112 nm nanopillar with a maximum intensity of ±70 V/m and ±200 V/m, respectively. Previous reports have suggested that the biphasic electric field is more efficient in neurostimulation.[26] Furthermore, the nanosecond pulsed electric field (nsPEF) stimulation has been under the limelight for the past two decades only. Although most applications have been found to be extremely efficient for tumor ablation and cancer therapies, there are several controversial views in terms of neurostimulation. Some reports suggest that nsPEF inhibits action potential in primary hippocampal neurons[49] while several groups have recently reported the focal stimulation efficiency of nsPEF on neurons.[50−52] Romanenko et al. have reported the generation of action potentials from a single pulse of 10 ns,[50] Casciola et al. reported activation of a peripheral nervous system by a 12 ns stimuli,[52] and Pakhomov et al. reported the threshold intensity for neuronal membrane excitation by a 200 nsPEF.[51] All these methods invove extremely complex pulse generator hardware. Even though the molecular mechanism associated with nsPEF neurostimulation is still skeptical, promising reports from several groups validate the potential of these SOTNS as a potential low-power implantable nanosecond neurostimulator.

3.3. Power Consumption and Device Performance of SOTNS. To validate the fact that SOTNS has better efficiency in terms of device power consumption over its CMOS analogues, the total power consumption and area overhead have been calculated and listed in Table 2. The AFM/FM layers of SOTNS have been considered to have resistances in parallel. For calculation purposes, 1 μm length section out of the total length of AFM has been considered (see Figure 2a). The terms current density (J, Am^{-2}) refers to current through the AFM only. The total current (I, mA) refers to the current through the entire device. The power efficiency for SOTNS has been calculated by the product of the square of the total current in SOTNS and the equivalent resistance of the AFM/FM bilayer (resistivity values for AFM and FM in Table 2 have been calculated from refs 53 and 54. Considering the average time for switching in the FM14-SOTNS and FM112-SOTNS nanodevices to be 2 and 3 ns, the power consumption of SkyNS was calculated as 6.34 μW and 313.5 μW, which is approximately 10^{13} times lower than commercialized TMS coils and 10^3 times lower than DBS electrodes. Even though magnetic microcoils for micromagnetic neurostimulation (μMS) have shown significant improvement in terms of the power of operation, they still consume 10 times more power in comparison to SOTNS. The calculations presented in Table 2 significantly emphasize the importance of spintronic nanodevices as the potential ultralow-power neurostimulators. Also as reported by Curiale et al.,[55] that for extremely short current pulse duration, <100 ns, the temperature is expected to rise by just 1 K only. Although, significant thermal effects occur when duration for charge current is greater than 100 ns, it is highly unlikely that SOTNS will be made to operate at durations so high in this range. Thus, we predict that rise in local temperature will have little to no effect on SOTNS device performance as a neurostimulator.

Table 2. Power of Device Operation and Area Overhead for SOTNS

parameters	description	values
FM nanopillar dimension	diameter × thickness	112 nm ×1 nm (14 nm ×1 nm)
AFM dimension	length × width × thickness	1 μm × 112 nm × 9 nm (1 μm × 14 nm × 9 nm)
J_C	charge current density	2.2×10^{12} A/m^2 (2.5×10^{12} A/m^2)
area of cross-section for nanopillar	circumference × thickness	351.68 nm^2 (43.96 nm^2)
area of cross-section AFM	width × thickness	126 nm^2
ρ_{PtMn}	resistivity of AFM	6.9×10^{-9} ohm−m
R_{PtMn}	resistance of AFM	54.76 ohm
ρ_{CoFeB}	resistivity of FM	105×10^{-8} ohm−m
R_{CoFeB}	resistance of FM	334.39 ohm (334.39 ohm)
R_{eq}	equivalent resistance	47.054 ohm
I	total current applied in this simulation	0.367 mA (2.581 mA)
P	power consumption	6.34 μW (313.5 μW)

4. CONCLUSIONS

To summarize, we have initially explored the feasibility of applying magnetic spintronic nanodevices for neuromodulation applications. An AFM/FM structure is employed for which the AFM layer supplies an in-plane exchange bias field on the adjacent FM layer and meanwhile generates SOT to enable deterministic switching of perpendicular magnetization. This current driven magnetization dynamics in SOTNS has no mechanically moving parts. Furthermore, the size of the SOTNS can be down to tens of nanometers. Thus, arrays of SOTNSs could be fabricated, integrated together, and patterned on a flexible substrate, which gives us much more flexible control of the neuromodulation. The magnetization dynamics of two AFM/FM structures were simulated using OOMMF: FM14-SOTNS and FM112-SOTNS, which are 1 nm thick FM nanopillars with diameters of 14 and 112 nm, respectively. The time evolutions of the charge current, Z-component magnetization in FM nanopillars, and calculated electric fields are plotted. During one magnetization switch cycle (from $+Z$ to $-Z$ direction or vice versa), the precessional motions of the magnetization in the FM nanopillar induce high frequency electric fields. As the FM nanopillar diameter increases from 14 to 112 nm, the magnitudes of the induced electric fields increase from tens of mV/mm to hundreds of mV/mm. In addition, the time duration of electric field in each neuromodulation cycle increases from 2 to 3 ns. Furthermore, SOTNS consumes a power within the range of 6.34−313.5 μW only.

The fields of neuroscience and neural engineering have seen rapid growth during the last few decades, especially in new fabrication and materials technologies to produce high density, miniaturized, and customized electrode arrays for sensing and stimulating neurons.[56−58] Nanometer-scale devices exploiting spintronics can be a key technology in this context. Spintronic nanodevices offer a plethora of novel mechanisms which can

DOI: 10.1021/acs.jpcc.9b07542
J. Phys. Chem. C 2019, 123, 24963−24972

be harnessed into new device paradigms with the potential to drive progress in the sensing and modulation of neuron activities. Other features of spintronic nanodevices for neuromodulations include tunable magnetic dynamics, low-power consumption, no wear out (no mechanical moving parts) during function cycles, and their magnetic/electric performances are not affected by the encapsulation of astrocytes or any other cells. In addition, over the past decade, there have been exciting developments in using polymer coatings (e.g., PEDOT), hydrogels, and surface modifications to improve the tissue and functional interaction of the nanodevices with the surrounding neurons. It can be foreseen that spintronic nanodevices along with neural engineering will enable more precise diagnostics and low-power therapeutics for brain disorders.

■ ASSOCIATED CONTENT

Supporting Information

The Supporting Information is available free of charge on the ACS Publications website at DOI: 10.1021/acs.jpcc.9b07542.

Numerical results of the critical switching current density as a function of demagnetization field in a nanopillar (PDF)

■ AUTHOR INFORMATION

Corresponding Authors

*E-mail: wuxx0803@umn.edu.

*E-mail: jpwang@umn.edu.

ORCID

Kai Wu: 0000-0002-9444-6112

Diqing Su: 0000-0002-5790-8744

Renata Saha: 0000-0002-0389-0083

Notes

The authors declare no competing financial interest.

■ ACKNOWLEDGMENTS

This study was financially supported by the Institute of Engineering in Medicine of the University of Minnesota through FY18 IEM Seed Grant Funding Program, National Science Foundation MRSEC facility program, the Distinguished McKnight University Professorship, Centennial Chair Professorship, Robert F Hartmann Endowed Chair, and UROP program from the University of Minnesota.

■ REFERENCES

(1) Dayal, V.; Limousin, P.; Foltynie, T. Subthalamic Nucleus Deep Brain Stimulation in Parkinson's Disease: The Effect of Varying Stimulation Parameters. *J. Parkinson's Dis.* **2017**, *7* (2), 235−245.

(2) Amon, A.; Alesch, F. Systems for Deep Brain Stimulation: Review of Technical Features. *J. Neural Transm.* **2017**, *124* (9), 1083−1091.

(3) Gimsa, J.; Habel, B.; Schreiber, U.; van Rienen, U.; Strauss, U.; Gimsa, U. Choosing Electrodes for Deep Brain Stimulation Experiments−Electrochemical Considerations. *J. Neurosci. Methods* **2005**, *142* (2), 251−265.

(4) Polikov, V. S.; Tresco, P. A.; Reichert, W. M. Response of Brain Tissue to Chronically Implanted Neural Electrodes. *J. Neurosci. Methods* **2005**, *148* (1), 1−18.

(5) Kim, Y.-T.; Hitchcock, R. W.; Bridge, M. J.; Tresco, P. A. Chronic Response of Adult Rat Brain Tissue to Implants Anchored to the Skull. *Biomaterials* **2004**, *25* (12), 2229−2237.

(6) Golestanirad, L.; Kirsch, J.; Bonmassar, G.; Downs, S.; Elahi, B.; Martin, A.; Iacono, M.-I.; Angelone, L. M.; Keil, B.; Wald, L. L.; Pilitsis, J. RF-Induced Heating in Tissue near Bilateral DBS Implants during MRI at 1.5 T and 3T: The Role of Surgical Lead Management. *NeuroImage* **2019**, *184*, 566−576.

(7) Iacono, M. I.; Makris, N.; Mainardi, L.; Angelone, L. M.; Bonmassar, G. MRI-Based Multiscale Model for Electromagnetic Analysis in the Human Head with Implanted DBS. *Comput. Math. Methods Med.* **2013**, *2013*, 1.

(8) Grehl, S.; Martina, D.; Goyenvalle, C.; Deng, Z. D.; Rodger, J.; Sherrard, R. M. Magnetic Stimulation: A Simple Stimulation Device to Deliver Defined Low Intensity Electromagnetic Fields. *Front. Neural Circuits* **2016**, *10*, 85.

(9) Janicak, P. G.; Dokucu, M. E. Transcranial Magnetic Stimulation for the Treatment of Major Depression. *Neuropsychiatr. Dis. Treat.* **2015**, *11*, 1549.

(10) Luber, B.; McClintock, S. M.; Lisanby, S. H. Applications of Transcranial Magnetic Stimulation and Magnetic Seizure Therapy in the Study and Treatment of Disorders Related to Cerebral Aging. *Dialogues Clin. Neurosci.* **2013**, *15* (1), 87−98.

(11) Golestanirad, L.; Gale, J. T.; Manzoor, N. F.; Park, H.-J.; Glait, L.; Haer, F.; Kaltenbach, J. A.; Bonmassar, G. Solenoidal Micro-magnetic Stimulation Enables Activation of Axons with Specific Orientation. *Front. Physiol.* **2018**, *9*, 724 DOI: 10.3389/fphys.2018.00724.

(12) Park, H.-J.; Bonmassar, G.; Kaltenbach, J. A.; Machado, A. G.; Manzoor, N. F.; Gale, J. T. Activation of the Central Nervous System Induced by Micro-Magnetic Stimulation. *Nat. Commun.* **2013**, *4*, 2463.

(13) Bonmassar, G.; Lee, S. W.; Freeman, D. K.; Polasek, M.; Fried, S. I.; Gale, J. T. Microscopic Magnetic Stimulation of Neural Tissue. *Nat. Commun.* **2012**, *3*, 921.

(14) Park, H.-J.; Seol, J. H.; Ku, J.; Kim, S. Computational Study on the Thermal Effects of Implantable Magnetic Stimulation Based on Planar Coils. *IEEE Trans. Biomed. Eng.* **2016**, *63* (1), 158−167.

(15) Wang, J.; Low, W. C.; Mahendra, D. Magnetic Nanostimulator and Nanosensor Array for Biological Material Stimulation and Sensing. U.S. Patent US20160303392A1, 2016.

(16) Saha, R.; Wu, K.; Su, D.; Wang, J.-P. Tunable Magnetic Skyrmions in Spintronic Nanostructures for Cellular-Level Magnetic Neurostimulation. *J. Phys. D: Appl. Phys.* **2019**, *52*, 465002.

(17) Tenforde, T. Biological Interactions of Extremely-Low-Frequency Electric and Magnetic Fields. *J. Electroanal. Chem. Interfacial Electrochem.* **1991**, *320* (1), 1−17.

(18) Liu, L.; Pai, C. F.; Li, Y.; Tseng, H. W.; Ralph, D. C.; Buhrman, R. A. Spin-Torque Switching with the Giant Spin Hall Effect of Tantalum. *Science* **2012**, *336* (6081), 555−558.

(19) Miron, I. M.; Garello, K.; Gaudin, G.; Zermatten, P.-J.; Costache, M. V.; Auffret, S.; Bandiera, S.; Rodmacq, B.; Schuhl, A.; Gambardella, P. Perpendicular Switching of a Single Ferromagnetic Layer Induced by In-Plane Current Injection. *Nature* **2011**, *476* (7359), 189.

(20) Lau, Y. C.; Betto, D.; Rode, K.; Coey, J. M.; Stamenov, P. Spin-Orbit Torque Switching without an External Field Using Interlayer Exchange Coupling. *Nat. Nanotechnol.* **2016**, *11* (9), 758−762.

(21) Oh, Y. W.; Chris Baek, S. H.; Kim, Y. M.; Lee, H. Y.; Lee, K. D.; Yang, C. G.; Park, E. S.; Lee, K. S.; Kim, K. W.; Go, G.; et al. Field-Free Switching of Perpendicular Magnetization through Spin-Orbit Torque in Antiferromagnet/Ferromagnet/Oxide Structures. *Nat. Nanotechnol.* **2016**, *11* (10), 878−884.

(22) Fukami, S.; Zhang, C.; DuttaGupta, S.; Kurenkov, A.; Ohno, H. Magnetization Switching by Spin−Orbit Torque in an Antiferromagnet−Ferromagnet Bilayer System. *Nat. Mater.* **2016**, *15* (5), 535.

(23) You, L.; Lee, O.; Bhowmik, D.; Labanowski, D.; Hong, J.; Bokor, J.; Salahuddin, S. Switching of Perpendicularly Polarized Nanomagnets with Spin Orbit Torque without an External Magnetic Field by Engineering a Tilted Anisotropy. *Proc. Natl. Acad. Sci. U. S. A.* **2015**, *112* (33), 10310−10315.

(24) Wang, M.; Cai, W.; Zhu, D.; Wang, Z.; Kan, J.; Zhao, Z.; Cao, K.; Wang, Z.; Zhang, Y.; Zhang, T.; Park, C.; Wang, J.-P.; Fert, A.; Zhao, W. Field-Free Switching of a Perpendicular Magnetic Tunnel

Junction through the Interplay of Spin−Orbit and Spin-Transfer Torques. *Nat. Electron.* **2018**, *1* (11), 582.
(25) Lee, K.-S.; Lee, S.-W.; Min, B.-C.; Lee, K.-J. Threshold Current for Switching of a Perpendicular Magnetic Layer Induced by Spin Hall Effect. *Appl. Phys. Lett.* **2013**, *102* (11), 112410.
(26) Panagopoulos, D. J.; Karabarbounis, A.; Margaritis, L. H. Mechanism for Action of Electromagnetic Fields on Cells. *Biochem. Biophys. Res. Commun.* **2002**, *298* (1), 95−102.
(27) Wise, K. D.; Angell, J. B.; Starr, A. An Integrated-Circuit Approach to Extracellular Microelectrodes. *IEEE Trans. Biomed. Eng.* **1970**, *BME-17* (3), 238−247.
(28) Wise, K. D.; Anderson, D. J.; Hetke, J. F.; Kipke, D. R.; Najafi, K. *Proc. IEEE* **2004**, *92* (1), 76−97.
(29) Ye, J.; Tang, S.; Meng, L.; Li, X.; Wen, X.; Chen, S.; Niu, L.; Li, X.; Qiu, W.; Hu, H.; Jiang, M.; Shang, S.; shu, Q.; Zheng, H.; Duan, S.; Li, Y. Ultrasonic Control of Neural Activity through Activation of the Mechanosensitive Channel MscL. *Nano Lett.* **2018**, *18* (7), 4148−4155.
(30) Tufail, Y.; Matyushov, A.; Baldwin, N.; Tauchmann, M. L.; Georges, J.; Yoshihiro, A.; Tillery, S. I. H.; Tyler, W. J. Transcranial Pulsed Ultrasound Stimulates Intact Brain Circuits. *Neuron* **2010**, *66* (5), 681−694.
(31) Avedisova, A.; Marachev, M. 2639−The Effectiveness of Agomelatine (Valdoxan) in the Treatment of Atypical Depression. *Eur. Psychiatry* **2013**, *28*, 1.
(32) Mount, C.; Downton, C. Alzheimer Disease: Progress or Profit? *Nat. Med.* **2006**, *12* (7), 780.
(33) Donahue, M. J. *OOMMF User's Guide, version 1.0*; NIST, 1999.
(34) Garello, K.; Miron, I. M.; Avci, C. O.; Freimuth, F.; Mokrousov, Y.; Blügel, S.; Auffret, S.; Boulle, O.; Gaudin, G.; Gambardella, P. Symmetry and Magnitude of Spin−Orbit Torques in Ferromagnetic Heterostructures. *Nat. Nanotechnol.* **2013**, *8* (8), 587.
(35) Emori, S.; Bauer, U.; Ahn, S.-M.; Martinez, E.; Beach, G. S. Current-Driven Dynamics of Chiral Ferromagnetic Domain Walls. *Nat. Mater.* **2013**, *12* (7), 611.
(36) Kim, J.; Sinha, J.; Hayashi, M.; Yamanouchi, M.; Fukami, S.; Suzuki, T.; Mitani, S.; Ohno, H. Layer Thickness Dependence of the Current-Induced Effective Field Vector in Ta| CoFeB| MgO. *Nat. Mater.* **2013**, *12* (3), 240.
(37) Zhang, C.; Fukami, S.; Sato, H.; Matsukura, F.; Ohno, H. Spin-Orbit Torque Induced Magnetization Switching in Nano-Scale Ta/CoFeB/MgO. *Appl. Phys. Lett.* **2015**, *107* (1), 012401.
(38) Zhang, W.; Jungfleisch, M. B.; Jiang, W.; Pearson, J. E.; Hoffmann, A.; Freimuth, F.; Mokrousov, Y. Spin Hall Effects in Metallic Antiferromagnets. *Phys. Rev. Lett.* **2014**, *113* (19), 196602.
(39) Chen, J.-Y.; DC, M.; Zhang, D.; Zhao, Z.; Li, M.; Wang, J.-P. Field-Free Spin-Orbit Torque Switching of Composite Perpendicular CoFeB/Gd/CoFeB Layers Utilized for Three-Terminal Magnetic Tunnel Junctions. *Appl. Phys. Lett.* **2017**, *111* (1), 012402.
(40) Zhang, W.; Jungfleisch, M. B.; Freimuth, F.; Jiang, W.; Sklenar, J.; Pearson, J. E.; Ketterson, J. B.; Mokrousov, Y.; Hoffmann, A. All-Electrical Manipulation of Magnetization Dynamics in a Ferromagnet by Antiferromagnets with Anisotropic Spin Hall Effects. *Phys. Rev. B: Condens. Matter Mater. Phys.* **2015**, *92* (14), 144405.
(41) Ou, Y.; Shi, S.; Ralph, D.; Buhrman, R. Strong Spin Hall Effect in the Antiferromagnet PtMn. *Phys. Rev. B: Condens. Matter Mater. Phys.* **2016**, *93* (22), 220405.
(42) DuttaGupta, S.; Kanemura, T.; Zhang, C.; Kurenkov, A.; Fukami, S.; Ohno, H. Spin-Orbit Torques and Dzyaloshinskii-Moriya Interaction in PtMn/[Co/Ni] Heterostructures. *Appl. Phys. Lett.* **2017**, *111* (18), 182412.
(43) Zhu, T.; Zhang, Q.; Yu, R. *Tuning Perpendicular Magnetic Anisotropy in the MgO/CoFeB/Ta Thin Films*; IEEE, 2015; pp 1−1.
(44) Liu, Y.; Hao, L.; Cao, J. Effect of Annealing Conditions on the Perpendicular Magnetic Anisotropy of Ta/CoFeB/MgO Multilayers. *AIP Adv.* **2016**, *6* (4), 045008.
(45) Yoshida, C.; Noshiro, H.; Yamazaki, Y.; Sugii, T.; Furuya, A.; Ataka, T.; Tanaka, T.; Uehara, Y. Electrical-Field and Spin-Transfer Torque Effects in CoFeB/MgO-Based Perpendicular Magnetic Tunnel Junction. *AIP Adv.* **2016**, *6* (5), 055816.
(46) Moretti, D.; DiFrancesco, M. L.; Sharma, P. P.; Dante, S.; Albisetti, E.; Monticelli, M.; Bertacco, R.; Petti, D.; Baldelli, P.; Benfenati, F. Biocompatibility of a Magnetic Tunnel Junction Sensor Array for the Detection of Neuronal Signals in Culture. *Front. Neurosci.* **2018**, *12*, 909.
(47) Rohart, S.; Thiaville, A. Skyrmion Confinement in Ultrathin Film Nanostructures in the Presence of Dzyaloshinskii-Moriya Interaction. *Phys. Rev. B: Condens. Matter Mater. Phys.* **2013**, *88* (18), 184422.
(48) Chen, B.; Lourembam, J.; Goolaup, S.; Lim, S. T. Field-Free Spin-Orbit Torque Switching of a Perpendicular Ferromagnet with Dzyaloshinskii-Moriya Interaction. *Appl. Phys. Lett.* **2019**, *114* (2), 022401.
(49) Roth, C. C.; Payne, J. A.; Kuipers, M. A.; Thompson, G. L.; Wilmink, G. J.; Ibey, B. L. *Impact of Nanosecond Pulsed Electric Fields on Primary Hippocampal Neurons*; International Society for Optics and Photonics, 2012; Vol. *8207*, p 820763.
(50) Romanenko, S.; Arnaud-Cormos, D.; Leveque, P.; O'Connor, R. P. *Ultrashort Pulsed Electric Fields Induce Action Potentials in Neurons When Applied at Axon Bundles*; IEEE, 2016; pp 1−5.
(51) Pakhomov, A. G.; Semenov, I.; Casciola, M.; Xiao, S. Neuronal Excitation and Permeabilization by 200-Ns Pulsed Electric Field: An Optical Membrane Potential Study with FluoVolt Dye. *Biochim. Biophys. Acta, Biomembr.* **2017**, *1859* (7), 1273−1281.
(52) Casciola, M.; Xiao, S.; Pakhomov, A. G. Damage-Free Peripheral Nerve Stimulation by 12-Ns Pulsed Electric Field. *Sci. Rep.* **2017**, *7* (1), 10453.
(53) Kastner, J.; Wassermann, E.; Matho, K.; Tholence, J. Low-Temperature Resistivity of Dilute PtMn Alloys. *J. Phys. F: Met. Phys.* **1978**, *8* (1), 103.
(54) Hao, Q.; Xiao, G. Giant Spin Hall Effect and Magnetotransport in a Ta/CoFeB/MgO Layered Structure: A Temperature Dependence Study. *Phys. Rev. B: Condens. Matter Mater. Phys.* **2015**, *91* (22), 224413.
(55) Curiale, J.; Lemaître, A.; Faini, G.; Jeudy, V. Track Heating Study for Current-Induced Domain Wall Motion Experiments. *Appl. Phys. Lett.* **2010**, *97* (24), 243505.
(56) Wise, K. D.; Najafi, K. Microfabrication Techniques for Integrated Sensors and Microsystems. *Science* **1991**, *254* (5036), 1335−1342.
(57) Banks, D. Neurotechnology. *Eng. Sci. Educ. J.* **1998**, *7* (3), 135−144.
(58) Pearce, T. M.; Williams, J. C. Microtechnology: Meet Neurobiology. *Lab Chip* **2007**, *7* (1), 30−40.

DOI: 10.1021/acs.jpcc.9b07542
J. Phys. Chem. C 2019, 123, 24963−24972